

Cite this: *Phys. Chem. Chem. Phys.*, 2011, **13**, 17163–17170

www.rsc.org/pccp

PAPER

# Pressure enhancement in carbon nanopores: a major confinement effect

Yun Long,<sup>a</sup> Jeremy C. Palmer,<sup>a</sup> Benoit Coasne,<sup>b</sup>  
Małgorzata Śliwiska-Bartkowiak<sup>c</sup> and Keith E. Gubbins<sup>\*a</sup>

Received 3rd May 2011, Accepted 4th August 2011

DOI: 10.1039/c1cp21407a

Phenomena that occur only at high pressures in bulk phases are often observed in nanopores, suggesting that the pressure in such confined phases is large. We report a molecular simulation study of the pressure tensor of an argon nanophase within slit-shaped carbon pores and show that the tangential pressure is positive and large, while the normal pressure can be positive or negative depending on pore width. We also show that small changes in the bulk pressure have a large effect on the tangential pressure, suggesting that it should be possible to control the latter over wide ranges in laboratory experiments.

## 1. Introduction

Nanophases confined within solids with pores of nanometer dimensions often exhibit physical and chemical properties that are dramatically different from those of the bulk material.<sup>1</sup> Such confinement effects are of fundamental interest across many fields, and result from the reduced dimensionality and the strong intermolecular forces between the molecules in the confined phase and the porous material. They find practical applications in areas as diverse as purification of water and air streams, heterogeneous catalysis, drug delivery, sensors, energy storage, in fabrication of nanomaterials such as nanowires, as insulators in microcircuits and as electrodes for fuel cells and supercapacitors.

Phenomena that occur only at very high pressures (*e.g.* thousands or tens of thousands of bars) in the bulk phase material are often observed to occur in the confined phase at pressures (the pressure of the bulk phase in equilibrium with the confined phase) that are orders of magnitude lower.<sup>2,3</sup> Examples of such phenomena include high pressure chemical reactions, high pressure solid phases, high pressure effects in solid-liquid equilibria and effects on spectral properties. The well-studied nitric oxide dimer reaction,  $2\text{NO} \leftrightarrow (\text{NO})_2$ , provides an illustration of the high pressure effect. In the bulk gas phase it has a yield of less than 1 mole% dimer at 300 K and 1 bar pressure, but in activated carbon fibers having an average pore width of 0.8 nm the yield of dimers is 99%, as measured by magnetic susceptibility.<sup>4</sup> Fourier transform infrared spectroscopy measurements of this reaction in

single-walled carbon nanotubes with a diameter of 1.35 nm similarly show 100% dimers<sup>5</sup> (Table 1), and molecular simulation results<sup>6</sup> for NO dimerization in slit-shaped carbon pores and carbon nanotubes are in qualitative agreement with these experiments. A simple thermodynamic calculation shows that dimer yields of 98–99 mole% would only be reached in the bulk phase at pressures between 12 000 and 15 000 bar at these temperatures. Numerous studies also observe high pressure phases in nanopores.<sup>7–13</sup> Liquid-solid transitions in nanophases confined between atomically-smooth mica surfaces in surface force apparatus experiments have been observed for several substances at temperatures well above their normal melting points,  $T_{\text{mp}}$ . Examples are shown in Table 2, and include cyclohexane<sup>7–9</sup> ( $T_{\text{mp}} = 279$  K) at 296 K (bulk phase freezes at  $\sim 440$  bar at 296 K) and *n*-dodecane<sup>10</sup> ( $T_{\text{mp}} = 263.4$  K) at 300 K (bulk phase freezes at  $\sim 1860$  bar at 300 K). Molecular simulations<sup>11</sup> for dodecane between mica surfaces are in agreement with the experimental data. Finally, we note several experimental small-angle X-ray scattering studies that show significant effects of the adsorption of a confined nanophase on the pore width and interlayer atomic spacing,<sup>12,13</sup> indicative of strong positive or negative pressure normal to the pore walls.

With the aim of providing fundamental understanding of these apparently unconnected effects in confined nanophases, we report a molecular simulation study of the pressure tensor for argon within a simple slit-pore model of a microporous carbon. Using semi-grand canonical Monte Carlo (SGCMC) simulation, we examine the effects of the extent of confinement (pore width), temperature, and bulk phase pressure on the density and pressure profiles, and on the radial distribution functions. We show that the tangential pressure,  $P_T$ , parallel to the walls is positive and reaches tens of thousands of bars locally at ambient bulk pressure, while the normal pressure,  $P_N$ , can be positive or negative, depending on the pore width, and is of the order of thousands of bars. We further find that the tangential pressure is sensitive to small changes in the bulk

<sup>a</sup> Department of Chemical and Biomolecular Engineering, North Carolina State University, Raleigh, NC 27695, USA. E-mail: keg@ncsu.edu; Fax: 919 513 2470; Tel: 1 919 513 0481

<sup>b</sup> Institut Charles Gerhardt Montpellier, CNRS (UMR 5253), Université de Montpellier 2 and CNRS (UMR 5253), 8 rue Ecole Normale, 34296, Montpellier, France

<sup>c</sup> Institute of Physics, Adam Mickiewicz University, Umultowska 85, 61-614 Poznan, Poland

**Table 1** Comparison of product mole fraction in bulk phase and in porous carbons for the NO dimerization reaction

Porous material	Pore size/nm	$T/K$	$(\text{NO})_2$ mole fraction	
			Bulk	Confined
ACF <sup>4</sup>	0.8	298–423	< 0.01	0.98–1.0
SWCNT <sup>5</sup>	1.35	103–136	≤ 0.01	1.0

**Table 2** Surface force apparatus results<sup>7–9</sup>

Substance	Pore width/nm	$T_{\text{mp}}/K$	$T_{\text{exp}}/K$	$P_{\text{freezing}}$ at $T_{\text{exp}}/\text{bar}$
cyclohexane	1–7	279	296	~440
<i>n</i> -dodecane	2.5–10	263.4	300	~1860

pressure, suggesting that it should be possible to control  $P_T$  over wide ranges in laboratory experiments. The normal pressure leads to changes in the pore width and graphene interlayer spacing during adsorption, as has been observed experimentally.<sup>12</sup>

The paper is arranged as follows. In section 2 we give a brief discussion of the conditions for thermodynamic and mechanical equilibrium in nanopores, as well as the equations for the pressure in inhomogeneous systems. In section 3 the model system used to investigate the local pressure tensor is described along with details of the calculations. In section 4, we present and discuss the results. Finally, in section 5, we summarize our findings and discuss related avenues of interest for future investigation.

## 2. Pressure tensor

Our system consists of a uniform bulk fluid phase (*bulk*) in thermodynamic and mechanical equilibrium with a confined nanophase (*pore*), as shown in Fig. 1. Thermodynamic equilibrium requires the temperature and chemical potential to be equal in the two phases:

$$\begin{aligned} T_{\text{bulk}} &= T_{\text{pore}} \\ \mu_{\text{bulk}} &= \mu_{\text{pore}} \end{aligned} \quad (1)$$

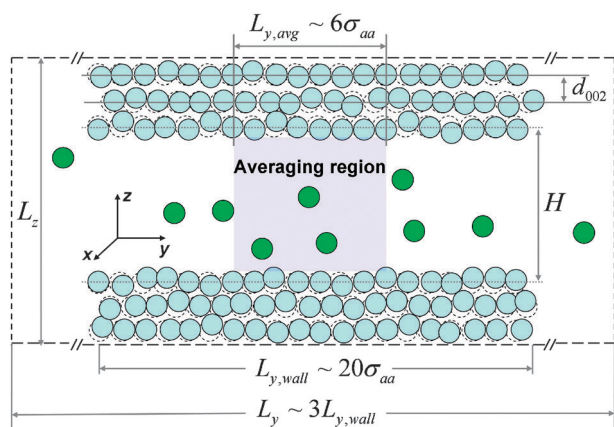


**Fig. 1** The simulation cell. The dark (green in color) circles represent adsorbate argon molecules, and the light (blue in color) circles represent carbon atoms. Dashed circles represent the equilibrium positions of carbons atoms. C atoms are shown at reduced scale for clarity.

The condition of mechanical equilibrium requires that there be, on average, no net momentum transfer once the system has reached equilibrium. For two homogeneous fluid phases separated by a planar interface this leads to equality of the scalar pressure in the two phases. In the confined nanophase, however, the pressure  $\mathbf{P}(\mathbf{r})$  is a second order tensor, while that in the bulk phase is a scalar,  $P_{\text{bulk}}$ .  $\mathbf{P}(\mathbf{r})$  has elements  $P_{\alpha\beta}(\mathbf{r})$ , that give the force per unit area in the  $\beta$ -direction acting on a surface element pointing in the  $\alpha$ -direction at point  $\mathbf{r}$ . Since there is no external field present in our system the mechanical equilibrium condition becomes:<sup>14</sup>

$$\nabla \cdot \mathbf{P}(\mathbf{r}) = 0. \quad (2)$$

Our slit pore system has axial symmetry about the  $z$ -axis and translational symmetry in the  $xy$  plane, so that  $P_{xx} = P_{yy} = P_T$  and  $P_{zz} = P_N$ . Moreover, mechanical equilibrium, eqn (2), requires that:

$$\begin{aligned} \frac{\partial P_T}{\partial x} &= \frac{\partial P_T}{\partial y} = 0 \\ \frac{\partial P_N}{\partial z} &= 0. \end{aligned} \quad (3)$$

Thus, the tangential pressure is independent of  $x$  and  $y$  but dependent on  $z$ , the distance from the walls, while the normal pressure is independent of  $x$ ,  $y$  and  $z$ , but not equal to the bulk phase pressure due to the intermolecular forces from the walls.

For a system of  $N$  spherical particles, an expression for the many-body pressure tensor can be rigorously derived from the microscopic law of momentum conservation.<sup>14,15</sup> In the case that the particles interact in a purely pair-wise fashion, the local pressure tensor is given by:

$$\mathbf{P}(\mathbf{r}) = \rho(\mathbf{r})k_B T \mathbf{1} - \frac{1}{2} \left\langle \sum_{i \neq j}^N \frac{d\mathbf{u}(\mathbf{r}_{ij})}{d\mathbf{r}_{ij}} \int_{C_{ij}} \delta(\mathbf{r} - \tilde{\ell}) d\tilde{\ell} \right\rangle, \quad (4)$$

where  $\rho(\mathbf{r})$  is the local particle density,  $\mathbf{1}$  is the unit tensor,  $u$  is the pair-wise intermolecular potential energy function,  $C_{ij}$  is an arbitrary contour from the center of mass position of particle  $i$ ,  $\mathbf{r}_i$ , to the center of mass position of particle  $j$ ,  $\mathbf{r}_{ij} = \mathbf{r}_j - \mathbf{r}_i$  and the brackets indicate that the quantity inside is ensemble-averaged. The first term on the right in eqn (4) is the kinetic contribution to the pressure tensor that arises from convective momentum transport across the surface elements, whereas the second term is the configurational contribution due to intermolecular forces between particles.

Eqn (4) is formally rigorous, but while the kinetic term is uniquely defined the configurational contribution is not, due to the arbitrary nature of the contour integral. Physically this means that there is no unique way of determining how forces acting between particles should be assigned to elements of the local pressure tensor. This is a consequence of the momentum flux being defined with respect to the gradient of the pressure tensor and not the pressure tensor itself.<sup>14,15</sup> However, we can make an operational definition of the configurational contribution to the pressure by choosing a particular path for the contour integral. The most natural choice is that of Irving and Kirkwood,<sup>16</sup> who chose the integration path to be a straight line along the vector  $\mathbf{r}_{ij}$ ,

$$\tilde{\ell}(\mathbf{r}_i, \mathbf{r}_j) = \lambda \mathbf{r}_{ij} + \mathbf{r}_i; \quad 0 \leq \lambda \leq 1. \quad (5)$$

With this choice substituted into eqn (4), the Irving–Kirkwood<sup>16</sup> (IK) expression for the pressure tensor is obtained,

$$\mathbf{P}_{IK}(\mathbf{r}) = \rho(\mathbf{r})k_B T \mathbf{1} - \frac{1}{2} \left\langle \sum_{i \neq j}^N \frac{\mathbf{r}_{ij} \mathbf{r}_{ij}}{r_{ij}} \frac{du(\mathbf{r}_{ij})}{dr_{ij}} \right. \\ \left. \times \int_0^1 d\lambda \delta(\mathbf{r}_i - \mathbf{r} + \lambda \mathbf{r}_{ij}) \right\rangle. \quad (6)$$

Alternatives to the IK contour have been proposed, the most noteworthy being that of Harasima.<sup>17</sup> Both methods yield the same result for the surface tension at planar interfaces.<sup>15</sup> However, in addition to being the most widely used and natural choice, only the IK definition has been shown to yield expressions for the pressure difference, surface tension and Tolman length that are consistent with those obtained using microscopic sum rules.<sup>18</sup> More seriously, the Harasima contour has been found to yield inconsistent and unphysical results when calculated using different coordinate systems.<sup>19</sup> For these reasons, we have used the IK definition of the pressure tensor for the calculations presented in this study.

The expression for the local pressure tensor provided by eqn (6) is amenable to evaluation in molecular simulation of complex systems. In practice, however, calculation of all the components of the pressure tensor is a cumbersome task, and the complexity of the results of such calculations would likely obscure physical interpretation for all but simple systems. As a result, application of eqn (6) is usually restricted to situations in which off-diagonal elements of the pressure tensor are zero ( $P_{\alpha\beta}(\mathbf{r}) = 0$  ( $\alpha \neq \beta$ )) due to the symmetry of the system. For example, at an infinite planar surface lying in the  $xy$ -plane, symmetric about the  $z$ -axis, there are only two unique non-zero components, a normal and a tangential component, as discussed above. Likewise, in spherically symmetric systems, only  $P_N(r) = P_{rr}(r)$  and  $P_T(r) = P_{\theta\theta}(r) = P_{\phi\phi}(r)$  need to be calculated. In systems with cylindrical symmetry, eqn (6) reduces to a slightly more complicated form, since all three diagonal components,  $P_{rr}(r)$ ,  $P_{\theta\theta}(r)$  and  $P_{zz}(r)$ , are non-zero and vary radially.<sup>20</sup>

### 3. Methods

Molecular simulation was used to study the local pressure tensor of argon confined in a model carbon slit-pore. Although the slit-pore model is a highly simplified approximation of the porous features found in many real materials,<sup>21</sup> it has played an essential role in the development of theoretical approaches for characterizing porous materials.<sup>22</sup> In addition, it also provides a unified context for achieving a fundamental understanding of the impact of various confinement effects<sup>1,3</sup> on adsorption,<sup>23</sup> transport,<sup>24</sup> chemical reaction<sup>25</sup> and poromechanics.<sup>26</sup> The slit-pore model is also capable of making quantitative predictions of the adsorptive properties of ordered carbon materials, such as graphitizable carbon blacks.<sup>27,28</sup> For the purposes of this study, it provides a well-established starting point for understanding pressure enhancement effects in confined systems in which eqn (6) may be readily evaluated.

Semi-grand canonical Monte Carlo simulations<sup>13,29</sup> in which the volume of the simulation cell,  $V$ , temperature,  $T$ , chemical potential of the adsorbate,  $\mu_a$ , and number of pore

wall atoms,  $N_w$ , are fixed, were used to study argon adsorption and the local pressure tensor in an atomistically-detailed, finite and flexible carbon slit-pore model. Since the pore is finite, the adsorbed phase is in direct physical contact with the bulk argon gas phase at temperature  $T_{bulk}$  and pressure  $P_{bulk}$  at both ends of the pore, thus ensuring that mechanical equilibrium is reached (eqn (2) and (3)). The usual Monte Carlo particle moves, and particle insertion and deletion attempts, assure that the system reaches thermal and chemical equilibrium (eqn (1)). As shown in Fig. 1, a rectangular simulation cell comprised of a slit-shaped carbon pore, symmetric about  $z = 0$ , was used. Opposing walls of the slit-pore each consisted of 3 layers of graphene that lay parallel to the  $xy$ -plane. During the simulations, the positions of the outermost graphene layers were kept fixed in space, but the two innermost graphene layers in each pore wall were permitted to move, thus allowing the effect of the confined nanophase on pore width and interlayer spacing to be studied. The dimensions of the simulation cell were  $L_x \times L_y \times L_z = L_{x,wall} \times (3 \times L_{y,wall}) \times (H_e + 5 \times d_{002,e})$ , where  $L_{x,wall} \times L_{y,wall} = 3.408 \text{ nm} \times 6.8866 \text{ nm}$  are the dimensions of the graphene layers. Here  $H_e$  is the width of the pore when empty, defined as the distance between the innermost graphene layers on the opposing wall surfaces, when at their equilibrium positions. The values for the graphene interlayer spacing when empty,  $d_{002,e} = 0.3395 \text{ nm}$ ,  $0.3405 \text{ nm}$  and  $0.3438 \text{ nm}$  at 87.3 K, 135 K and 300 K, respectively, were obtained by running an initial set of simulations of an empty pore. Carbon atoms in a given graphene layer were arranged on a hexagonal lattice, with a C–C bond length of 0.142 nm. The atoms in all layers were connected to their lattice positions by a harmonic potential, with a spring constant,  $k_s = 18.1 \text{ N/m}$ , that was obtained by matching to the AIREBO potential of Stuart and coworkers for carbon.<sup>30</sup>

Interactions between carbon atoms in different graphene layers were modeled using the Lennard-Jones (LJ) potential with Steele's parameters,<sup>31</sup>  $\epsilon_{cc}/k_B = 28.0 \text{ K}$  and  $\sigma_{cc} = 0.340 \text{ nm}$ . Argon–argon and argon–carbon interactions were also modeled using the LJ potential. The LJ parameters used for argon,<sup>32</sup>  $\epsilon_{aa}/k_B = 119.8 \text{ K}$  and  $\sigma_{aa} = 0.3405 \text{ nm}$ , are widely used and have been shown to accurately predict the vapor-liquid equilibrium envelope.<sup>33</sup> Parameters for the argon–carbon interactions were estimated using the usual Lorentz-Berthelot combining rules (*i.e.*,  $\epsilon_{ac} = \sqrt{\epsilon_{aa}\epsilon_{cc}}$  and  $\sigma_{ac} = (\sigma_{aa} + \sigma_{cc})/2$ ). All LJ interactions were truncated at  $r_c = 5\sigma$  and intermolecular distances were evaluated according to the minimum image convention. Periodic boundary conditions were applied in the  $x$ -direction, and hard-wall boundary conditions were used for the  $y$  and  $z$  directions.

Adsorption isotherms for argon at 87.3 K (normal boiling point of argon), 135 K (under, but near the critical point) and 300 K (ambient temperature and supercritical), were simulated over a wide range of bulk pressures in the slit-pore model. To obtain an appropriate relationship between the chemical potential and the bulk pressure of argon over the range of state conditions examined, the LJ equation of state of Johnson *et al.*<sup>34</sup> was used. The SGC MC simulations were run for a total of  $1.2 \times 10^8$  MC moves at each chemical potential, with statistics collected over the second half of the simulations. Insertions, deletions and displacements of argon atoms were

attempted with equal probability. Displacements of carbon atoms about their lattice sites were attempted with the same frequency as the argon trial moves, while the layer displacement attempts along the  $z$ -axis were made with an average frequency of 1/400 MC trial moves. To expedite equilibration, final atomic configurations were used as starting configurations for the simulations performed at subsequent chemical potentials along the adsorption isotherms.

Evaluation of the local pressure tensor inside the slit-pore was carried out at regular intervals during the production phase of the SGCMC simulations, with a minimum of 30 000 samples used to compute ensemble averages at each state point. The calculations were restricted to an averaging region deep inside the pore, far away from the pore-bulk interface, as depicted in Fig. 1. Within this averaging region, it was assumed that spatial variations in the  $xy$ -plane could be neglected and that the pressure tensor components only vary along the  $z$ -axis normal to the surface of the pore walls. This allowed for calculations to be performed inside the averaging region using expressions for the local tangential and normal components of the pressure tensor derived by Walton *et al.*<sup>35</sup> from eqn (6) for an infinite interface in the  $xy$ -plane,

$$P_{T,IK}(z) = \rho(z)k_B T - \frac{1}{4A} \left\langle \sum_{i \neq j} \frac{x_{ij}^2 + y_{ij}^2}{r_{ij}} \frac{1}{|z_{ij}|} \frac{du(r_{ij})}{dr_{ij}} \right. \\ \left. \times \theta\left(\frac{z-z_i}{z_{ij}}\right) \theta\left(\frac{z_j-z}{z_{ij}}\right) \right\rangle \quad (7)$$

and

$$P_{N,IK}(z) = \rho(z)k_B T - \frac{1}{2A} \left\langle \sum_{i \neq j} \frac{z_{ij}^2}{r_{ij}} \frac{1}{|z_{ij}|} \frac{du(r_{ij})}{dr_{ij}} \right. \\ \left. \times \theta\left(\frac{z-z_i}{z_{ij}}\right) \theta\left(\frac{z_j-z}{z_{ij}}\right) \right\rangle, \quad (8)$$

respectively. In eqn (7) and (8),  $A$  is the area of the surface,  $\theta(x)$  is the unit step function and  $x_{ij}$ ,  $y_{ij}$  and  $z_{ij}$  are components of the intermolecular separation vector  $\mathbf{r}_{ij}$ . The expression in eqn (7) results from averaging the two in-plane components,  $P_{T,IK}(z) = (P_{xx}(z) + P_{yy}(z))/2$ , while  $P_{N,IK}(z) = P_{zz}(z)$ , as discussed in the previous section. For a planar interface, the condition of mechanical equilibrium, eqn (3), requires  $P_{N,IK}(z) = \text{constant}$ , independent of  $z$ . Thus, in principle, eqn (8) only needs to be evaluated at one point along the  $z$ -axis in order to calculate the normal component of the pressure tensor. In this study, eqn (7) and (8) were evaluated every 0.01 nm along the  $z$ -axis of the slit-pore. The normal component of the pressure tensor was calculated by averaging the values taken along the  $z$ -axis. The standard error of the mean for the normal component served as a check to ensure that the simulations were properly equilibrated and that the sampling procedures used to calculate the pressure tensor yielded results within the desired statistical uncertainty of 5%.

## 4. Results and discussion

Adsorption isotherm and pressure tensor calculations were carried out in model carbon slit-pores with reduced pore widths,

$H_c^* = H_c/\sigma_{aa}$ , ranging from 2.0 to 8.0 (0.68 to 2.72 nm). These pore sizes were chosen because they encompass the typical range of micropore widths found in materials such as nanoporous carbons.<sup>36,37</sup> Density and pressure profiles are shown in Fig. 2, together with snapshots of argon adsorbed in pores of different widths at 87.3 K and 1 bar bulk pressure.

The density profiles exhibit the well known layering effect of confinement, with 1, 2, 4 and 6 layers of argon molecules for  $H_c^* = 2.0, 3.0, 4.5$  and  $7.0$ , respectively, which are also shown in the accompanying snapshots. Very high local densities are observed at the center of the contact layers, with  $\rho^* = \rho\sigma_{aa}^3$  rising to over 7 for all these pores. Examination of the confined layers of argon shows that the molecules have adopted a face-centered cubic (fcc) structure, as in the solid phase of bulk argon. At 87.3 K the fcc crystal phase occurs only at pressures above several hundred bars for bulk argon.<sup>38</sup>

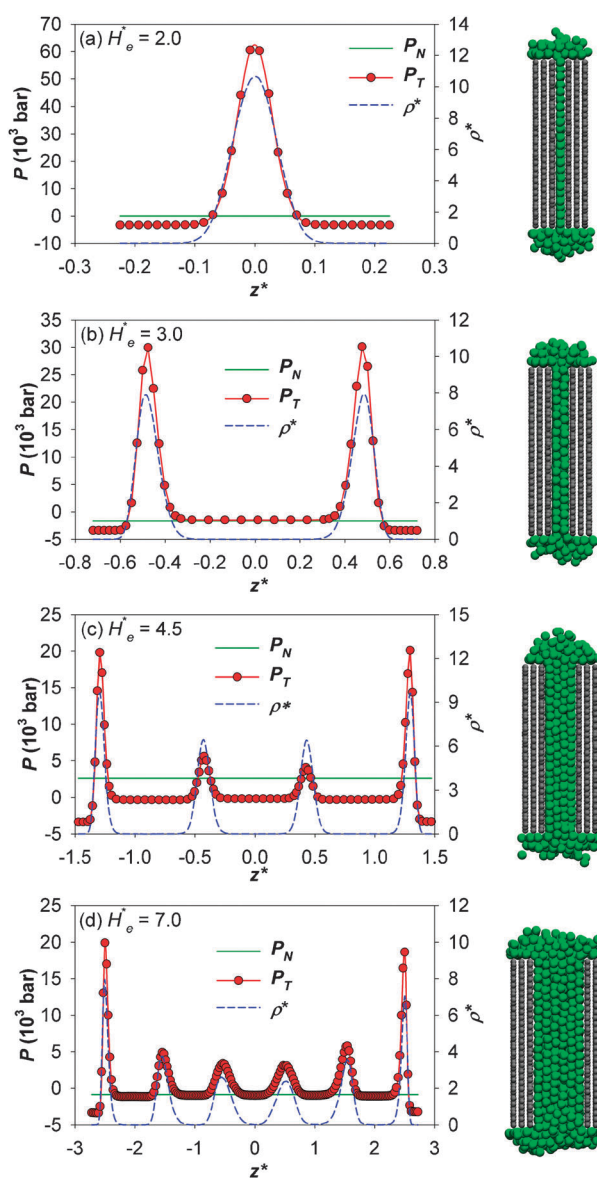


**Fig. 2** The density and pressure profiles and snapshots at 87.3 K and 1 bar bulk pressure for pores of reduced widths,  $H_c^*$ , of 2.0, 3.0, 4.5 and 7.0, respectively. Carbon atoms are shown at reduced scale for clarity.

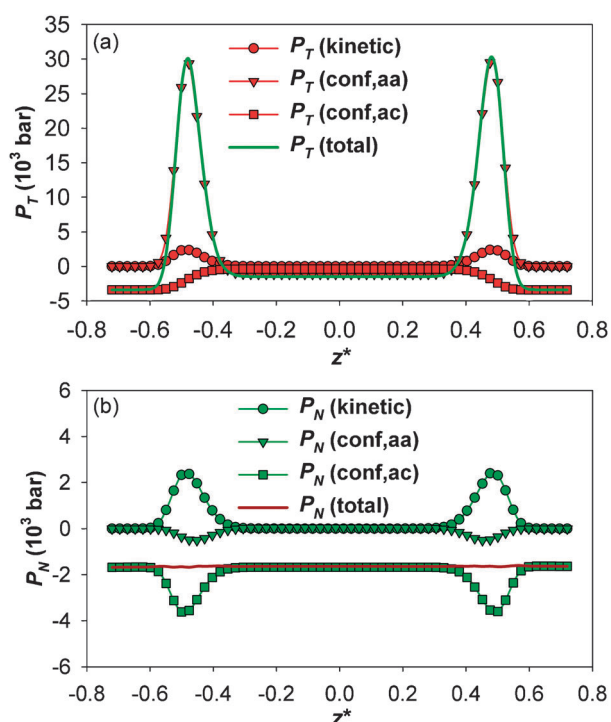


**Fig. 3** Decomposition of the (a) tangential and (b) normal pressure tensor profiles into the kinetic contribution and the argon-argon and argon-carbon configurational contributions for  $H_e^* = 3.0$  at 87.3 K and 1 bar bulk pressure.

The tangential pressure profile follows that of the density, with very high pressures of over 20 000 bar at the contact layer peaks for all pore widths. For  $H_e^* = 2.0$ , only a single layer of argon can be accommodated, and the tangential pressure at the peak is approximately 60 000 bar. The normal pressure  $P_N$ , while smaller, oscillates with pore width due to oscillations in the average density in the pore. We note that  $P_N$  is simply related to the solvation (or disjoining) pressure by  $P_{\text{solvation}} = P_N - P_{\text{bulk}}$ .

The contribution of the kinetic and configurational terms to the pressure profiles (see eqn (4)) are shown in Fig. 3a and b for  $H_e^* = 3.0$  at 87.3 K and 1 bar bulk pressure. In each case, the argon-argon and argon-carbon contributions of the configurational part of the pressure tensor profiles are shown separately.

As is evident from Fig. 3a, the tangential pressure profile is strongly dominated by the configurational contribution arising from argon-argon interactions. This large, positive contribution that arises in the contact layers indicates the presence of strong repulsive forces between argon molecules within the layer. The argon-carbon contribution is slightly negative and decreases to a value of  $\sim -2500$  bar in the contact layers. For a pore of infinite extent in the  $xy$ -plane, eqn (7) suggests that the argon-carbon contribution to the tangential pressure should be zero due to the symmetry of the system. However, for the atomically-detailed, finite slit-pore model presented here, this symmetry is not strictly maintained due to the structure of the pore walls. This leads to a slightly negative argon-carbon contribution to the tangential pressure tensor. We note that a similar negative contribution would

also be expected in any real material, since the porous features are finite and structured. This negative contribution to the tangential pressure is roughly offset by the positive kinetic contribution at this temperature, which peaks at approximately 2500 bar at the density maxima. The kinetic part of the normal pressure profile is the same as in the tangential pressure profile, again with a peak height of  $\sim 2500$  bar. However, both the argon-argon and argon-carbon configurational contributions are negative, which reflects the fact that the forces are attractive and that the system is in tension, rather than compression, along the normal direction. Figs. 2 and 3b show that mechanical equilibrium is maintained, with  $P_N$  constant in each case, within the statistical uncertainty of the calculations, as required by eqn (3).

The high in-pore tangential pressures arise from the confinement of the nanophase and the strong attraction between the carbon walls and argon molecules, which force the adsorbed phase into highly compressed layers. To demonstrate this, we calculated the in-plane ( $xy$ -plane) radial distribution function,  $g(r)$ , which gives the probability distribution of finding two argon molecules at a separation distance,  $r$ , within the same layer. The in-plane  $g(r)$  for the contact layers of argon in the  $H_e^* = 3.0$  pore is shown in Fig. 4a at the boiling point of argon, 87.3 K and 1 bar, and also at ambient temperature and 3990 bar. For reference,  $g(r)$  is also shown for bulk liquid argon at 87.3 K. The first peak in  $g(r)$  corresponds to the most probable nearest neighbor distance in a given layer. At both state conditions examined, this distance is found to be significantly smaller than in bulk liquid argon at 87.3 K and is in the steeply rising repulsive region of the intermolecular pair force, as shown in Fig. 4b. This large and positive repulsive force gives rise directly to the observed large tangential pressures. Such compression has been previously reported for strongly attractive surfaces.<sup>39</sup> Preliminary calculations indicate that similar pressure tensor profiles and neighbor distances are also found in slit-pores modeled using Steele's (10,4,3) potential.<sup>31</sup> This suggests that the compression of the adsorbed layers is not strongly affected by the atomistic nature or flexibility of the pore walls, although these features are essential in capturing the deformation of the pores in response to these large forces. However, we note that for hard spheres against a hard wall, where attractive forces are absent, there is little or no enhancement of the tangential pressure.<sup>40</sup>

It is of interest to note that this situation is the opposite of that observed in gas-liquid interfaces, where the most probable separation between neighboring molecules in the  $xy$ -plane is *greater* than that in the bulk liquid. Thus, in our MC simulations of the gas-liquid interface for argon at its normal boiling point, we find that the most probable argon-argon separation distance is  $r^* = 1.17$ , significantly greater than for bulk liquid argon ( $r^* = 1.12$ ), so that the average pair force is negative (attractive), as it must be to produce a surface tension (see also ref. 41). The tangential pressure in this case is therefore negative, being approximately  $-80$  bar near the center of the interface.

The effect of varying the bulk pressure and temperature is shown in Fig. 5 for the  $H_e^* = 3.0$  pore. At 87.3 K, argon adsorption starts to occur at  $P_{\text{bulk}} \sim 2 \times 10^{-5}$  bar, and at somewhat higher pressures there are two jumps in the density

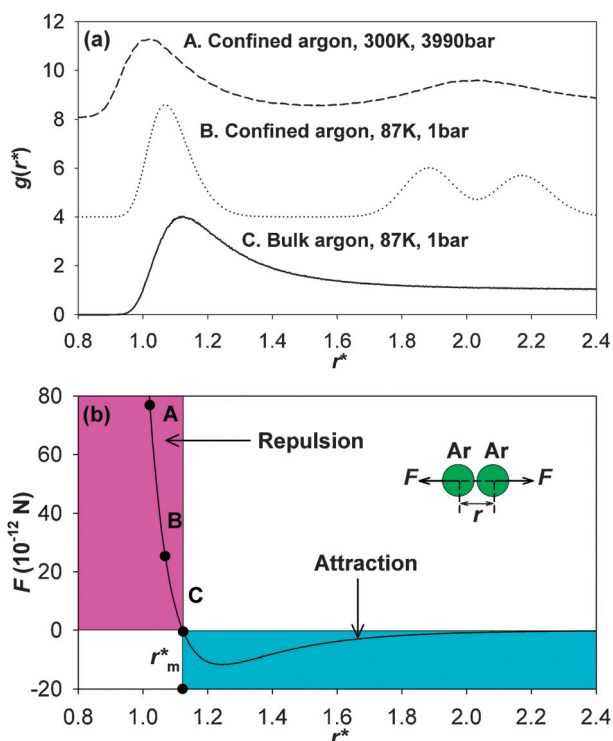


**Fig. 4** (a) Radial distribution function in the  $xy$ -plane for confined argon at 300 K and 3990 bar bulk pressure (A, dashed line) and at 87.3 K and 1 bar bulk pressure (B, dotted line), and the isotropic radial distribution function for bulk argon at the boiling point at 87.3 K (C, solid line). (b) The intermolecular pair force between two argon atoms,  $F$ , with the most probable nearest neighbor separation distances shown for the three cases illustrated in (a).

and in the peak value of the tangential pressure ( $P_{T,peak}$ ) corresponding to phase transitions from a gas-like to a liquid-like pore phase (at  $P_{bulk} \sim 6.2 \times 10^{-5}$  bar) and from a liquid-like to a fcc crystal pore phase (at  $P_{bulk} \sim 1.2 \times 10^{-4}$  bar). In addition to the peak value of tangential pressure,  $P_{T,peak}$ , the value averaged across the pore,  $P_{T,avg} = \int_{-H_c/2}^{H_c/2} P_T(z) f(z) dz$ , is also shown, where the probability density at  $z$  is  $f(z) = \rho(z) / \int \rho(z) dz$ . Both are observed to increase rapidly with  $P_{bulk}$ , following the increase in density, whereas  $P_N$  is only slightly affected. At 87.3 K the pressure enhancement,  $P_{T,peak}/P_{bulk}$ , is very large, being more than 7 orders of magnitude at  $P_{bulk} \sim 10^{-4}$  bar and falling to over 4 orders of magnitude at  $P_{bulk} \sim 1$  bar. As the temperature is increased, first to 135 K and then to 300 K, the nanophase capillary condensation transition vanishes (these temperatures are above the pore critical temperature) and there is no evidence of a liquid–solid transition, as shown in Fig. 5b and c. The kinetic contribution to the pressure tensor components becomes relatively more important at these higher temperatures, and this reduces the pressure enhancement,  $P_{T,peak}/P_{bulk}$ , considerably, to about three orders and one order of magnitude at 135 K and 300 K, respectively.

The normal pressure oscillates in sign as the empty pore width,  $H_c^*$ , is increased (Fig. 6). Such oscillations in  $P_N$  are observed in surface force measurements<sup>7,8</sup> as well as in simulations and theoretical calculations,<sup>42</sup> and are well-known to arise from density oscillations in the pore that result from the

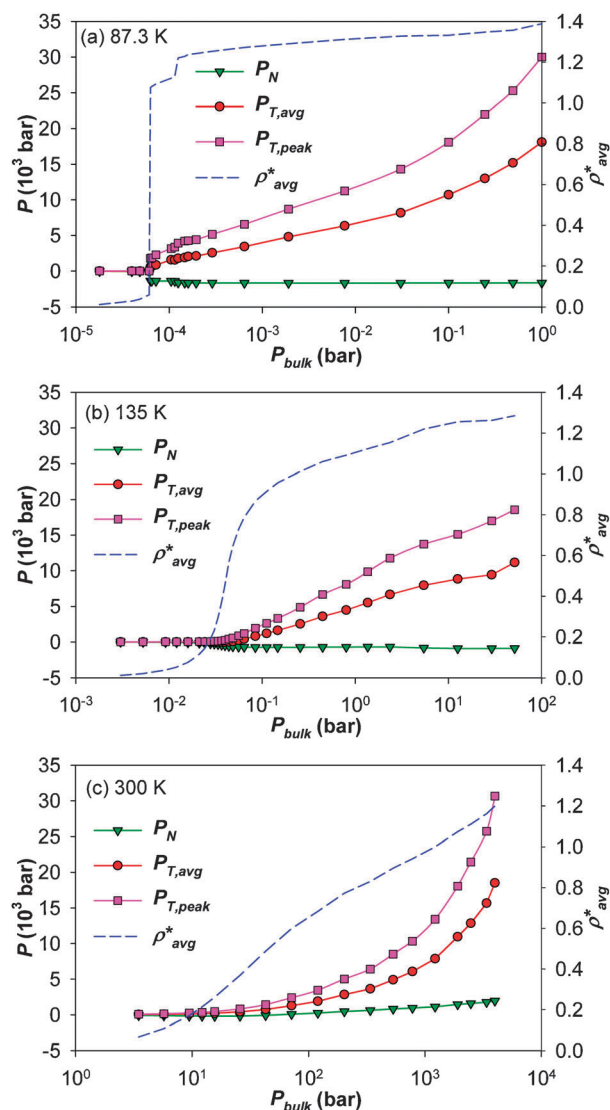


**Fig. 5** The average in-pore density and pressure of argon as a function of bulk pressure at 87.3 K, 135 K and 300 K, respectively, for the pore of reduced width of  $H_c^* = 3.0$ .

layered structure of the adsorbed phase. For example, for a pore with an empty width of  $H_c^* = 2.0$  only one layer of adsorbed argon can be accommodated, and increasing  $H_c^*$  further does not allow the formation of another adsorbed layer to begin until  $H_c^* \sim 2.4$ . Since additional argon molecules cannot adsorb, increasing the pore width from 2.0 to 2.4 reduces the in-pore density, resulting in a decrease in the normal pressure. At  $H_c^* \sim 2.4$ , the pore is wide enough so that a second layer of argon can begin to form, which causes an increase in the density and normal pressure. The density and normal pressure peak when the pore is just wide enough to accommodate a complete second layer of argon ( $H_c^* \sim 2.7$ ), and further increases in pore width leads to another decrease in density until a third layer of argon can start to form. Thus, the oscillations follow the formation of adsorbed layers as the pore width is increased. The period of the oscillations is approximately equal to the distance between molecules in adjacent layers, which is close to the LJ diameter of argon,  $\sigma_{aa} = 0.34$  nm.

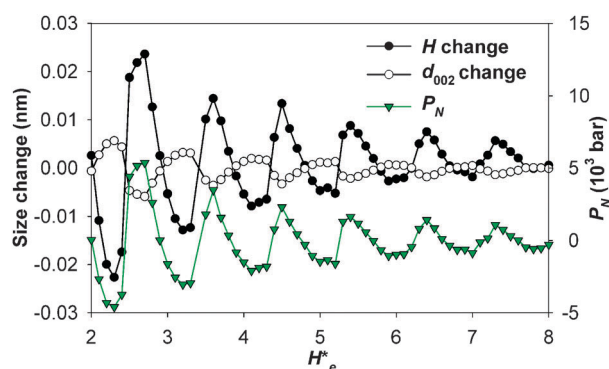


**Fig. 6** Normal pressure (right vertical axis), and changes to the empty pore width and graphene interlayer spacing  $d_{002}$  (left vertical axis) at 87.3 K and 1.0 bar bulk pressure.

Positive and negative oscillations of the normal pressure indicate that the system is in compression and tension, respectively, in the direction normal to the pore walls. This results in an expansion or contraction of the pore, as illustrated in Fig. 6. For smaller pore widths, changes in the pore width and interlayer spacing are approximately in the range  $\pm 0.02$  and  $\pm 0.005$  nm, respectively. As the pore width increases, smaller changes are observed due to the decay in the oscillations of the normal pressure. The magnitude of these changes, and of the normal pressures, are consistent with the experimentally known value of Young's modulus<sup>43,44</sup> for graphite (in the direction normal to the basal plane), which is  $E_{\perp} = P_N/(\Delta d_{002}/d_{002,e}) \approx 36.5$  GPa, where  $\Delta d_{002}$  is the change in the interlayer spacing due to adsorption. Taking 0.003 as a typical value of the latter quantity (see Fig. 6) gives a  $P_N$  value of 3285 bar, in qualitative agreement with the results for the normal pressure. We note that similar results have also been reported by Do *et al.*<sup>45</sup> for argon adsorption in a slit-pore with atomically-smooth, movable walls modeled using a modified Steele potential.<sup>31</sup>

Such mechanical deformation of adsorbent materials during sorption has recently received considerable attention. In highly flexible materials, such as metal-organic frameworks, mechanical forces arising from the adsorbed guest phase have been observed to cause a dramatic reversible collapse of the porous structure, resulting in deformation-induced sorption hysteresis.<sup>46</sup> In more rigid materials, such as mesoporous silica SBA-15, more subtle deformation has been observed in both experiment and simulation.<sup>13</sup> Nevertheless, even these smaller deformations are found to have a significant impact on adsorption behavior.<sup>13</sup> We note that the changes observed in Fig. 6 are qualitatively similar to those observed in diffraction experiments on activated carbons,<sup>12</sup> although the magnitudes of the changes observed experimentally are larger than those found in our simulations. This difference is to be expected, since activated carbons have a density of  $\sim 1.6$  g cm<sup>-3</sup>, much lower than for graphite ( $\rho_m \sim 2.23$  g cm<sup>-3</sup>), and this less dense structure is expected to lead to more deformation.

## 5. Conclusions

In summary, our calculations show that very high tangential and normal pressures are expected in carbon micropores and

small mesopores. These high in-pore pressures provide a unifying explanation for a wide range of previously unconnected experimental observations, including the occurrences of high pressure phases and high pressure reactions in carbons, and could provide a route to connect the behavior of the confined phase to that of the bulk phase. Such a connection could prove useful as a guide to future experimental studies of high pressure phenomena in nanoporous carbons. A further important finding is that relatively small changes in the bulk pressure (and to a lesser extent, the temperature) have a very large effect on the in-pore pressure. This sensitivity to the bulk phase pressure provides an explanation of the large effect of bulk pressure on the melting curve for confined phases that has been observed in molecular simulations.<sup>47,48</sup> This also suggests that it should be possible to experimentally observe a range of high pressure phenomena by simply varying the bulk pressure.

## Acknowledgements

It is a pleasure to thank Professor Katsumi Kaneko for helpful discussions of high pressure effects in nanopores and Dr. Joshua D. Moore for comments on the manuscript. We thank the National Science Foundation (grant no. CBET-0932658) for support of this research. Computational time was provided through a Teragrid Research Allocation by the U.S. National Science Foundation (grant No. CHE080046N).

## Notes and references

- 1 K. E. Gubbins, Y. C. Liu, J. D. Moore and J. C. Palmer, *Phys. Chem. Chem. Phys.*, 2011, **13**, 58–85.
- 2 C. Alba-Simionesco, B. Coasne, G. Dosseh, G. Dudziak, K. E. Gubbins, R. Radhakrishnan and M. Śliwinka-Bartkowiak, *J. Phys.: Condens. Matter*, 2006, **18**, R15–R68.
- 3 L. D. Gelb, K. E. Gubbins, R. Radhakrishnan and M. Śliwinka-Bartkowiak, *Rep. Prog. Phys.*, 1999, **62**, 1573–1659.
- 4 K. Kaneko, N. Fukuzaki, K. Kakei, T. Suzuki and S. Ozeki, *Langmuir*, 1989, **5**, 960–965.
- 5 O. Byl, P. Kondratyuk and J. T. Yates, *J. Phys. Chem. B*, 2003, **107**, 4277–4279.
- 6 C. H. Turner, J. K. Johnson and K. E. Gubbins, *J. Chem. Phys.*, 2001, **114**, 1851–1859.
- 7 J. Klein and E. Kumacheva, *Science*, 1995, **269**, 816–819.
- 8 J. Klein and E. Kumacheva, *J. Chem. Phys.*, 1998, **108**, 6996–7009.
- 9 E. Kumacheva and J. Klein, *J. Chem. Phys.*, 1998, **108**, 7010–7022.
- 10 H. W. Hu, G. A. Carson and S. Granick, *Phys. Rev. Lett.*, 1991, **66**, 2758–2761.
- 11 S. T. Cui, C. McCabe, P. T. Cummings and H. D. Cochran, *J. Chem. Phys.*, 2003, **118**, 8941–8944.
- 12 Y. Fujiwara, K. Nishikawa, T. Iijima and K. Kaneko, *J. Chem. Soc., Faraday Trans.*, 1991, **87**, 2763–2768.
- 13 G. Gunther, J. Prass, O. Paris and M. Schoen, *Phys. Rev. Lett.*, 2008, **101**, 086104.
- 14 C. G. Gray, K. E. Gubbins and C. G. Joslin, *Oxford University Press*, Sec. 8.3, Oxford, 2011.
- 15 P. Schofield and J. R. Henderson, *Proc. R. Soc. London, Ser. A*, 1982, **379**, 231–246.
- 16 J. H. Irving and J. G. Kirkwood, *J. Chem. Phys.*, 1950, **18**, 817–829.
- 17 A. Harasima, *Adv. Chem. Phys.*, 1958, **1**, 203.
- 18 E. M. Blokhuis and D. Bedeaux, *J. Chem. Phys.*, 1992, **97**, 3576–3586.
- 19 B. Hafskjold and T. Ikeshoji, *Phys. Rev. E: Stat. Phys., Plasmas, Fluids, Relat. Interdiscip. Top.*, 2002, **66**, 011203.

- 20 O. H. S. Ollila, H. J. Risselada, M. Louhivuori, E. Lindahl, I. Vattulainen and S. J. Marrink, *Phys. Rev. Lett.*, 2009, **102**, 078101.
- 21 J. C. Palmer, J. D. Moore, J. K. Brennan and K. E. Gubbins, *J. Phys. Chem. Lett.*, 2011, **2**, 165–169.
- 22 P. I. Ravikovitch, A. Vishnyakov, R. Russo and A. V. Neimark, *Langmuir*, 2000, **16**, 2311–2320.
- 23 R. F. Cracknell, D. Nicholson and N. Quirke, *Mol. Phys.*, 1993, **80**, 885–897.
- 24 Q. Cai, A. Buts, N. A. Seaton and M. J. Biggs, *Chem. Eng. Sci.*, 2008, **63**, 3319–3327.
- 25 C. H. Turner, J. K. Brennan, M. Lisal, W. R. Smith, J. K. Johnson and K. E. Gubbins, *Mol. Simul.*, 2008, **34**, 119–146.
- 26 K. Yang, X. C. Lu, Y. Z. Lin and A. V. Neimark, *Energy Fuels*, 2010, **24**, 5955–5964.
- 27 D. D. Do and H. D. Do, *Langmuir*, 2004, **20**, 10889–10899.
- 28 D. D. Do and H. D. Do, *J. Phys. Chem. B*, 2005, **109**, 19288–19295.
- 29 D. A. Kofke and E. D. Glandt, *Mol. Phys.*, 1988, **64**, 1105–1131.
- 30 S. J. Stuart, A. B. Tutein and J. A. Harrison, *J. Chem. Phys.*, 2000, **112**, 6472–6486.
- 31 W. A. Steele, *Surf. Sci.*, 1973, **36**, 317–352.
- 32 C. R. Fuselier, J. C. Raich and N. S. Gillis, *Surf. Sci.*, 1980, **92**, 667–680.
- 33 D. D. Do, L. Herrera, C. Y. Fan, A. Wongkoblap and D. Nicholson, *Adsorption*, 2009, **16**, 3–15.
- 34 J. K. Johnson, J. A. Zollweg and K. E. Gubbins, *Mol. Phys.*, 1993, **78**, 591–618.
- 35 J. P. R. B. Walton, D. J. Tildesley, J. S. Rowlinson and J. R. Henderson, *Mol. Phys.*, 1983, **48**, 1357–1368.
- 36 A. V. Neimark, Y. Z. Lin, P. I. Ravikovitch and M. Thommes, *Carbon*, 2009, **47**, 1617–1628.
- 37 J. C. Palmer, A. Llobet, S. H. Yeon, J. E. Fischer, Y. Shi, Y. Gogotsi and K. E. Gubbins, *Carbon*, 2010, **48**, 1116–1123.
- 38 R. G. Crafton, *Phys. Lett. A*, 1971, **36**, 121–122.
- 39 T. E. Wetzel, J. S. Erickson, P. S. Donohue, C. L. Charniak, G. L. Aranovich and M. D. Donohue, *J. Chem. Phys.*, 2004, **120**, 11765–11774.
- 40 J. R. Henderson and F. Van Swol, *Mol. Phys.*, 1984, **51**, 991–1010.
- 41 D. J. Lee, M. M. Telo da Gama and K. E. Gubbins, *Mol. Phys.*, 1984, **53**, 1113–1130.
- 42 P. B. Balbuena, D. Berry and K. E. Gubbins, *J. Phys. Chem.*, 1993, **97**, 937–943.
- 43 O. L. Blakslee, *J. Appl. Phys.*, 1970, **41**, 3373.
- 44 E. J. Seldin and C. W. Nezbeda, *J. Appl. Phys.*, 1970, **41**, 3389.
- 45 D. D. Do, D. Nicholson and H. D. Do, *J. Phys. Chem. C*, 2008, **112**, 14075–14089.
- 46 A. V. Neimark, F. X. Coudert, A. Boutin and A. H. Fuchs, *J. Phys. Chem. Lett.*, 2010, **1**, 445–449.
- 47 B. Coasne, J. Czwartos, M. Śliwinska-Bartkowiak and K. E. Gubbins, *J. Phys. Chem. B*, 2009, **113**, 13874–13881.
- 48 M. Miyahara, H. Kanda, M. Shibao and K. Higashitani, *J. Chem. Phys.*, 2000, **112**, 9909–9916.